

# Narrow- $K$ -Band Observations of the GJ 1214 System

Knicole D. Colón<sup>1</sup>, Eric Gaidos<sup>1</sup>

## ABSTRACT

GJ 1214 is a nearby M dwarf star that hosts a transiting super-Earth-size planet, making this system an excellent target for atmospheric studies. Most studies find that the transmission spectrum of GJ 1214b is flat, which favors either a high mean molecular weight or cloudy/hazy hydrogen (H) rich atmosphere model. Photometry at short wavelengths ( $< 0.7 \mu\text{m}$ ) and in the  $K$ -band can discriminate the most between these different atmosphere models for GJ 1214b, but current observations do not have sufficiently high precision. We present photometry of seven transits of GJ 1214b through a narrow  $K$ -band ( $2.141 \mu\text{m}$ ) filter with the Wide Field Camera on the 3.8 m United Kingdom Infrared Telescope. Our photometric precision is typically  $1.7 \times 10^{-3}$  (for a single transit), comparable with other ground-based observations of GJ 1214b. We measure a planet-star radius ratio of  $0.1158 \pm 0.0013$ , which, along with other studies, also supports a flat transmission spectrum for GJ 1214b. Since this does not exclude a scenario where GJ 1214b has a H-rich envelope with heavy elements that are sequestered below a cloud/haze layer, we compare  $K$ -band observations with models of  $\text{H}_2$  collision-induced absorption in an atmosphere for a range of temperatures. While we find no evidence for deviation from a flat spectrum (slope  $s = 0.0016 \pm 0.0038$ ), an  $\text{H}_2$  dominated upper atmosphere ( $< 60 \text{ mbar}$ ) cannot be excluded. More precise observations at  $< 0.7 \mu\text{m}$  and in the  $K$ -band as well as a uniform analysis of all published data would be useful for establishing more robust limits on atmosphere models for GJ 1214b.

*Subject headings:* planetary systems — planets and satellites: atmospheres — techniques: photometric

---

<sup>1</sup>Department of Geology and Geophysics, University of Hawai'i at Manoa, Honolulu, HI 96822; colonk@hawaii.edu

## 1. Introduction

To date, approximately 300 planets have been confirmed to transit their host star(s), and the *Kepler*<sup>1</sup> mission has discovered over 3500 additional transiting planet candidates. About 65 transiting planets (which have both a measured mass and radius) are considered to be in either the “super-Earth” ( $1 \lesssim R \lesssim 2 R_{\oplus}$ ) or “mini-Neptune” ( $2 \lesssim R \lesssim 4 R_{\oplus}$ ) regime, but less than a handful of these orbit nearby stars (Schneider et al. 2011). Planets like GJ 1214b, a  $\sim 2.7 R_{\oplus}$  transiting planet discovered around a nearby  $\sim 0.2 R_{\odot}$  M dwarf star by the MEarth ground-based transit survey (Charbonneau et al. 2009), are therefore of great interest for understanding the difference between Earth-like planets, “super-Earths”, and “mini-Neptunes.”

Planets in the super-Earth/mini-Neptune regime occupy a location in the planetary mass-radius diagram that allows for diverse interior compositions (Rogers & Seager 2010). However, it may be possible to constrain the overall bulk composition of these planets by characterizing the planet’s atmosphere. Models suggest that GJ 1214b contains a significant amount of hydrogen (H) and helium (He) based on its low mean density (approximately one-third that of Earth; Miller-Ricci & Fortney 2010). Valencia et al. (2013) constrained the fraction of H and He in GJ 1214b using a model of its interior and evolution. They conclude that there is some amount of H/He present and that the bulk amount of H/He may be up to 7% by mass (similar to Neptune). While this is only a small fraction, it suggests that GJ 1214b likely has *some* amount of H/He in its atmosphere. Since H has a large scale height due to its low molecular weight, even with a small amount of H in the atmosphere the upper atmosphere (i.e. a small distance above the homopause) can easily be H-dominated (Pierrehumbert 2010). Thus, if GJ 1214b is differentiated, then ice and rock will be concentrated in the interior and the concentration of H/He in the surrounding atmosphere could be much higher than 7%.

Many groups have studied its atmosphere by transmission spectroscopy or spectrophotometry (e.g., Bean et al. 2010, 2011; Berta et al. 2011; Croll et al. 2011; Crossfield et al. 2011; Désert et al. 2011; Berta et al. 2012; de Mooij et al. 2012; Murgas et al. 2012; Narita et al. 2012; Fraine et al. 2013; de Mooij et al. 2013; Narita et al. 2013; Teske et al. 2013) while others have continued improving models of its atmosphere (e.g., Benneke & Seager 2012; Heng & Kopparla 2012; Howe & Burrows 2012; Menou 2012; Miller-Ricci Kempton et al. 2012; Morley et al. 2013; Valencia et al. 2013). Figure 1 presents measurements of the planet-star radius ratio (or simply, the radius ratio,  $R_p/R_*$ ) of GJ 1214b, along with two representative atmosphere models from Howe & Burrows (2012). GJ 1214b has a largely

---

<sup>1</sup><http://kepler.nasa.gov/>

41 flat, featureless spectrum, which supports an atmosphere with a high molecular weight and  
 42 small scale height, and/or a strongly scattering layer (clouds or aerosols) (e.g., Berta et al.  
 43 2012). However, published observations at  $< 0.7 \mu\text{m}$  and in the  $K$ -band ( $\sim 1.9\text{--}2.5 \mu\text{m}$ ) as  
 44 yet cannot discriminate between these two scenarios. Different observations from Bean et al.  
 45 (2011), Carter et al. (2011), Kundurthy et al. (2011), de Mooij et al. (2012), Murgas et al.  
 46 (2012), Narita et al. (2013), and de Mooij et al. (2013) disagree as to whether or not there  
 47 is a rise in the spectrum at  $< 0.7 \mu\text{m}$  due to Rayleigh scattering. In the  $K_s$ -band, obser-  
 48 vations from Croll et al. (2011) have been interpreted as showing a deviation from a flat  
 49 spectrum, suggesting a lower mean molecular weight atmosphere, while Bean et al. (2011),  
 50 de Mooij et al. (2012), Narita et al. (2012), and Narita et al. (2013) find a flat spectrum.  
 51 The disagreement could be a result of the use of slightly different bandpasses combined with  
 52 telluric effects at the edges of the  $K$  passband, so a  $K$ -band filter that avoids the edges of the  
 53 bandpass could help resolve the disagreement between these observations and help determine  
 54 whether GJ 1214b has a high mean molecular weight atmosphere or a cloudy/hazy H-rich  
 55 atmosphere.

56 In one of the latest of many model analyses of the data, Howe & Burrows (2012) pre-  
 57 sented a suite of atmosphere models for GJ 1214b. They ultimately selected five models  
 58 that they deemed to best fit the published data, with three models of a solar-abundance  
 59 atmosphere (two with hazes with different particle sizes and densities and one with a uni-  
 60 formly opaque cloud layer) and two of an atmosphere of 1%  $\text{H}_2\text{O}$  and 99%  $\text{N}_2$  plus either  
 61 haze or no haze. They ruled out several models including a H-rich atmosphere with no haze,  
 62 a H-rich atmosphere with a haze of smaller ( $\sim 0.01 \mu\text{m}$ ) tholin particles, as well as a H-poor  
 63 atmosphere with major sources of absorption other than water. The model that best fits  
 64 the short-wavelength rise (at  $< 0.7 \mu\text{m}$ ; Figure 1) is a solar composition atmosphere with a  
 65 (somewhat arbitrary) tholin haze layer having a particle size of  $0.1 \mu\text{m}$  and extending over  
 66 pressures of 10-0.1 mbar. This model is also the best fit to the  $K$ -band data, but only if  
 67 the observations from Croll et al. (2011) are correct over the observations from Bean et al.  
 68 (2011), de Mooij et al. (2012), Narita et al. (2012), and Narita et al. (2013), since a flat  
 69 spectrum in the  $K$ -band is inconsistent with a rise at short wavelengths. Howe & Burrows  
 70 (2012) conclude that if the rise at short wavelengths is valid, GJ 1214b should have a H-rich  
 71 atmosphere (albeit with some cloud or haze layer) rather than being composed primarily of  
 72 heavier molecules like water or nitrogen.

73 In this paper, we investigated the scenario of a H-rich atmosphere with a high cloud/aerosol  
 74 layer using narrow- $K$ -band observations of transits of GJ 1214b. We present observations  
 75 of seven transits of GJ 1214b through a narrow-band filter centered at the  $2.141 \mu\text{m}$  1-0  
 76 S(1) vibrational line of  $\text{H}_2$  (hereafter, referred to simply as the  $\text{H}_2$  filter). We used our  
 77 observations to (1) help resolve the disagreement between  $K$ -band measurements published

78 to date and (2) test if there is any spectral structure in the  $K$ -band that was missed by  
 79 the broad-band observations. Specifically, we (1) compared published  $K$ -band data to test  
 80 if the disagreement between  $K$ -band measurements is the result of subtle differences in the  
 81 bandpasses used convolved with not-so-subtle differences in the spectrum of the planet and  
 82 telluric absorption/emission that were not previously appreciated, and (2) compared  $K$ -  
 83 band data with a model of  $H_2$  collision-induced absorption in an atmosphere for a range of  
 84 temperatures.

85 We describe our observations and data reduction in Section 2. In Section 3, we present  
 86 our light curve analysis and models. We present our results in Section 4, and in Section 5 we  
 87 compare our results with published  $K$ -band observations, compare the data with models of a  
 88 H-rich atmosphere, investigate variability in the stellar spectrum due to  $H_2$ , and discuss the  
 89 effects of different systematics on our results. In Section 6, we summarize our conclusions  
 90 and offer suggestions for future work.

## 91 2. Observations and Data Reduction

92 We acquired photometry of seven transits of GJ 1214b between August 2011 and July  
 93 2012 with the Wide Field CAMera (WFCAM) on the 3.8 m United Kingdom InfraRed  
 94 Telescope (UKIRT) (Casali et al. 2001), located at the Mauna Kea Observatory in Hawaii.  
 95 WFCAM is a near-infrared wide field imager consisting of 4 Rockwell Hawaii-II (HgCdTe  
 96  $2048 \times 2048$ ) 0.4 arcsec pixel arrays. Each individual camera covers a field of  $13.65' \times 13.65'$ ,  
 97 and the total field of view (FOV) is 0.75 square degrees. A narrow-band filter centered on  
 98 the fundamental  $H_2$  vibrational line [S(1)  $\nu = 1 \rightarrow 0$ ] at  $2.141 \mu\text{m}$  (FWHM =  $0.021 \mu\text{m}$ ) was  
 99 used for all observations. This filter probes wavelengths at which previous observations are  
 100 in disagreement (Section 1) and minimizes systematic variations from Earth’s atmosphere.  
 101 In Figure 2, we compare the transmission profile of the  $H_2$  filter to the broad-band  $K_s$   
 102 filter [the same filter used by Croll et al. (2011) on the Wide-field InfraRed Camera on the  
 103 Canada-France-Hawaii Telescope] and the atmosphere above Mauna Kea Observatory (at  
 104 an airmass of 1 and with a water vapor column of 1.2 mm).<sup>2</sup> Because it is so narrow, the  $H_2$   
 105 filter is an optimal filter to avoid atmospheric effects (compared to the broader  $K_s$  filter).

106 In Table 1, we present details of each transit observation. All observations were per-  
 107 formed in service mode. An exposure time of 60 s was used for each integration, with a  
 108 typical dead time between exposures of  $\sim 2$ -3 s. The observation epochs (at mid-exposure)

---

<sup>2</sup>These data, produced using the program IRTRANS4, were obtained from the UKIRT worldwide web pages; <http://www.jach.hawaii.edu/UKIRT/astronomy/utis/atmos-index.html>

109 were extracted from the FITS header for each image. The telescope was intentionally de-  
 110 focused to avoid saturation and to spread the stellar PSF over many pixels to minimize  
 111 error from an imperfect flat-field correction of the detector response. Due to the amount  
 112 of defocus, the telescope auto-guider was not able to function properly. As a result, a drift  
 113 of 45-52 pixels in the position of the target centroid occurred during the 2011 observations.  
 114 For the 2012 observations, the telescope operator routinely adjusted the guider to keep the  
 115 defocused guide star centered in the guider acquisition window. A centroid drift of less than  
 116 9 pixels was maintained during the 2012 observations.

117 We reduced all images using software written in GDL.<sup>3</sup> While all images taken with  
 118 WFCAM are processed through a pipeline operated by the Cambridge Astronomical Survey  
 119 Unit (CASU), we opted to process our images separately to ensure accurate calibration and  
 120 photometry that was as precise as possible. The procedures were illumination correction,  
 121 dark current correction, and flat fielding prior to performing circular aperture photometry,  
 122 sky subtraction, and finally a radial distortion correction.

123 The illumination correction rectified each image for residual systematics, which are most  
 124 likely caused by either low-level non-linearity in the detectors, scattered light in the camera,  
 125 and/or spatially dependent PSF corrections.<sup>4</sup> Illumination correction tables are measured  
 126 monthly as a function of spatial location in the array. Since illumination correction tables  
 127 are only available for broad-band filters, we used the *K*-band tables as a proxy for the H<sub>2</sub>  
 128 filter. For the dark current and flat-field correction, we used darks taken the night of each  
 129 observation and monthly twilight flats taken with the H<sub>2</sub> filter. The appropriate flats from  
 130 a given month were used. Circular aperture photometry was performed with radii = 8, 10,  
 131 12, 14, 16, 18 pixels (3.2, 4.0, 4.8, 5.6, 6.4, 7.2 arcsec). In our analysis we ultimately used  
 132 the aperture that gave the best photometric performance (Section 3.2). An annulus of 25 -  
 133 30 pixels (10 - 12 arcsec) was used for sky subtraction.

134 Finally, a radial distortion correction was applied to the sky-subtracted flux measured  
 135 within a given aperture to account for non-negligible field distortion in WFCAM, a result of  
 136 its extremely large FOV. Specifically, photometry of sources near the edge of the FOV have  
 137 a systematic error of up to 0.02 mag. We computed the corrected flux,  $F_{corr}$ , from

$$F_{corr} = \frac{F(1 + k_3 r^2)}{1 + 3k_3 r^2}, \quad (1)$$

---

<sup>3</sup>GNU Data Language; <http://gnudatalanguage.sourceforge.net/>

<sup>4</sup><http://apm49.ast.cam.ac.uk/surveys-projects/wfcam/technical/photometry>

138 where  $F$  is the sky-subtracted flux measured within a given aperture,  $k_3$  is the coefficient  
 139 of the third order polynomial term in the radial distortion equation and is approximately -60  
 140  $\text{radian}^{-2}$  in the  $K$ -band (Hodgkin et al. 2009, and references therein), and  $r$  is the distance  
 141 of a star relative to the center of the optical system in radians. The corrected flux for the  
 142 target and each comparison star was used to generate the light curves (Section 3).

### 143 3. Analysis

#### 144 3.1. Selection of Comparison Stars

145 Thanks to the large FOV covered by WFCAM, we could select among numerous compar-  
 146 ison stars for relative photometry. We selected comparison stars that are of similar brightness  
 147 to GJ 1214 and that do not appear to be intrinsically variable. We also used colors to select  
 148 dwarf stars over giants and that are as close as possible to GJ 1214 in spectral type.

149 We downloaded  $J$ ,  $H$ , and  $K$  magnitudes from the 2MASS catalog (Skrutskie et al.  
 150 2006) and proper motions from the PPMXL catalog (Roeser et al. 2010) for all stars in the  
 151 vicinity (within 30 arcmin) of GJ 1214. We also downloaded  $V$  magnitudes from the Fourth  
 152 U.S. Naval Observatory CCD Astrograph Catalog (Zacharias et al. 2013). We imposed a  
 153 magnitude cut in  $K$ -band so that the reference stars were no more than 0.5 mag brighter  
 154 and 2 mag fainter than GJ 1214 ( $K = 8.782$ ). Figure 3 is a color-color diagram of all stars  
 155 that meet our magnitude criteria. Not all these stars are actually located in the FOV, since  
 156 WFCAM has four cameras, and there are gaps of 12.83 arcmin between the different cameras.

157 We selected reference stars from those shown in Figure 3 based on three different crite-  
 158 ria. We first selected eight stars that were more likely to be M dwarf stars based on color  
 159 criteria from Lépine & Gaidos (2011). Additional reference stars were selected based on  
 160 their proximity to a 2MASS main-sequence locus from Stead & Hoare (2011) and a locus for  
 161 K7 - M9.5 spectral types (Cutri et al. 2003).<sup>5</sup> Specifically, we selected stars in two regions  
 162 of color space, marked by the two boxes in Figure 3. These regions were also selected to  
 163 avoid the giant locus.<sup>6</sup> We identified three additional stars that fit this color criteria (and  
 164 that also were in the FOV). Finally, we computed the magnitude of the proper motion for  
 165 each star shown in Figure 3 (using proper motions from the PPMXL catalog). Following  
 166 Lépine & Gaidos (2011), we computed the reduced proper motion,  $H_V$ , as

---

<sup>5</sup>[http://www.pas.rochester.edu/~emamajek/memo\\_colors.html](http://www.pas.rochester.edu/~emamajek/memo_colors.html)

<sup>6</sup>[http://www.ast.leeds.ac.uk/~phy2j2s/Intrinsic\\_Stead10.pdf](http://www.ast.leeds.ac.uk/~phy2j2s/Intrinsic_Stead10.pdf)

$$H_V = V + 5 \log \mu + 5. \quad (2)$$

167 We then applied the constraint from Lépine & Gaidos (2011) to separate M dwarfs from  
 168 giants based on

$$H_V > 2.2(V - J) + 2.0. \quad (3)$$

169 We found that all stars in Figure 3 met this criterion. Therefore, to maximize the  
 170 number of optimal comparison stars, we chose to select additional stars with the highest  
 171 proper motions of the sample. Of the five stars with the highest proper motions (excluding  
 172 GJ 1214), only one was actually located within our FOV (i.e. not in a gap between cameras).  
 173 We added this star to our reference ensemble, bringing the total number of comparison stars  
 174 to 12.

175 A preliminary visual examination of the light curve of each reference star (the flux of  
 176 a given reference star divided by the total flux of the remaining reference stars) revealed  
 177 that four of the twelve stars were potentially variable (i.e. the light curves displayed possible  
 178 periodic fluctuations). For completeness, we considered all 12 reference stars when generating  
 179 light curves for GJ 1214. The number of reference stars ultimately included in the light curve  
 180 analysis varied between two and ten depending on which combination of references produced  
 181 the lowest scatter in each set of baseline (out-of-transit) data.

### 182 3.2. Generating the Light Curves

183 Light curves were generated from each data set by computing the relative flux ratio, i.e.  
 184 the target signal divided by the total weighted signal of an ensemble of reference stars. Due  
 185 to varying weather conditions and the intrinsic variability of some of the reference stars, the  
 186 reference ensemble was composed of different stars for each set of observations. To determine  
 187 which reference stars would be included in each ensemble, the rms of each reference star’s  
 188 signal was compared to an imposed photometric precision threshold (set to slightly different  
 189 values for each night to include an adequate number of reference stars, with a typical value  
 190 of  $8 \times 10^{-3}$ ). The stars that had an rms that exceeded the threshold were excluded from the  
 191 reference signal, and the remaining stars had their signals weighted (based on the rms of  
 192 each individual reference signal) when computing the combined ensemble reference signal.

193 Normalized light curves were generated for each photometric aperture by dividing the  
 194 relative flux ratio by the median relative flux ratio measured in the out-of-transit data. We

195 considered the resulting out-of-transit rms scatter as measured in each aperture and for each  
 196 night of observations, and we chose the aperture that gave the smallest scatter in a given  
 197 night.

198 Each light curve was then regressed against target centroid position, airmass, and peak  
 199 counts (per pixel) and a linear trend removed. In Figure 4, we show the light curve from  
 200 August 24, 2011 prior to detrending, along with the parameters used for detrending. This  
 201 light curve has a notable negative deviation after mid-transit, which we discuss in Section  
 202 5.4. We also tested correcting against variations in the absolute flux of the target and the  
 203 variance of the flux of the target, but we found that these additional corrections resulted in  
 204 a negligible change in the flux ratios.

205 We discarded some June 16, 2012 data due to an incorrect defocus setting and saturation  
 206 (Section 2), as well as some points that were unexplained extreme outliers ( $> 3\sigma$  from the  
 207 mean of either the baseline data or the data at the bottom of the transit). We discarded  
 208 one data point from the August 24, 2011 observations and 28 points from the June 16, 2012  
 209 observations. We then fit transit models to the light curve data, as described in the next  
 210 section.

### 211 3.3. Transit Models

212 To measure  $R_p/R_*$  we fit transit models to our seven transit light curves using the  
 213 Transit Analysis Package (TAP), a publicly available IDL code (Gazak et al. 2012).<sup>7</sup> TAP  
 214 fits limb-darkened transit light curves using EXOFAST (Eastman et al. 2013) to calculate  
 215 the model of Mandel & Agol (2002), along with a combination of Bayesian and Markov  
 216 Chain Monte Carlo (MCMC) techniques. TAP also employs a wavelet-based likelihood  
 217 function (Carter & Winn 2009) to robustly estimate parameter uncertainties by fitting both  
 218 uncorrelated (“white”) and correlated (“red”) noise. A quadratic limb darkening law was  
 219 used, so in the models described below, linear and quadratic ( $\mu_1$  and  $\mu_2$ ) limb darkening  
 220 coefficients are included.

221 We modeled all seven transits simultaneously, using five MCMC chains with lengths  
 222 of 100,000 links each, and keeping the following parameters fixed at a single value for all  
 223 transits: orbital period ( $P$ ), inclination ( $i$ ), scaled semi-major axis ( $a/R_*$ ), and the limb  
 224 darkening coefficients ( $\mu_1$  and  $\mu_2$ ). (We assumed a circular orbit.) The mid-transit time, as  
 225 well as the white and red noise, was individually fitted for each transit. To obtain  $R_p/R_*$

---

<sup>7</sup><http://ifa.hawaii.edu/users/zgazak/IfA/TAP.html>



226 we (i) fit individual transit light curves and (ii) fit the combined light curves of all transits.  
 227 The fixed parameters we used are given in Table 2. The  $K$ -band limb darkening parameters  
 228 are from Claret & Bloemen (2011) for a star with  $T_{\text{eff}} = 3000$  K and  $\log(g) = 5$  and are the  
 229 same as those used by Narita et al. (2012).

230 In Figure 5, we present the seven individual light curves. Figure 6 shows the combined  
 231 light curve (composed by phasing each of the individual light curves) and the best-fit model  
 232 for case (ii), where we fit a single  $R_p/R_*$  to all transits. We base our primary conclusions  
 233 on the results from this case. However, we discuss the individually measured radius ratios  
 234 in Section 4 and the effects of fixing versus fitting the limb darkening parameters and  $a/R_*$   
 235 in further detail in Section 5.5.

## 236 4. Results

237 In Table 3 we present the best-fit radius ratio, mid-transit time, white noise, and red  
 238 noise measured for each individual transit. We also include the best-fit radius ratio based on  
 239 fitting all seven transits together. Since TAP fits for correlated (red) noise, the uncertainties  
 240 on the fitted parameters should be conservative. This was also pointed out by Teske et al.  
 241 (2013), who compared results from TAP with results from other light curve fitting software.  
 242 The correlated noise is discussed in further detail in Section 5.4.

243 We find that all transit times deviate from the predicted ephemeris (from Berta et al.  
 244 2012) by less than 29 s and are consistent with a linear ephemeris. We also find that the  
 245 fitted values for the white noise are generally consistent with the rms scatter in each transit  
 246 light curve (Section 5.3), which suggests that the red noise may be smaller than the values  
 247 measured by TAP. We present the individual best-fit radius ratios in Figure 7. They are  
 248 all consistent with the combined best-fit radius ratio ( $0.1158 \pm 0.0013$ ). The radius ratio  
 249 measured for the fifth transit observation (June 16, 2012) has the largest uncertainty, but it  
 250 is still consistent with those measured from the other individual transits. The photometry of  
 251 this particular transit was of inferior quality than the other transit observations (Figure 5),  
 252 likely due in part to the presence of mixed thin and thick clouds throughout the observations.

253 In Figure 8, we present the results of our analysis along with other  $K$ -band measurements  
 254 of the radius ratio for GJ 1214b. We find that our best-fit radius ratio is consistent with  
 255 the majority of other published values and supports a flat absorption spectrum for the  
 256 atmosphere of GJ 1214b with a slope  $s = 0.0016 \pm 0.0038$  [excluding “outlying” points from  
 257 Croll et al. (2011) and de Mooij et al. (2012)]. We discuss this result further in Section 5.1.

## 5. Discussion

### 5.1. Comparison of $K$ -Band Observations

Our measurements are inconsistent with the conclusion of Croll et al. (2011), that GJ 1214b has a low mean molecular weight atmosphere. One  $K_s$ -band measurement from de Mooij et al. (2012) also supports the data from Croll et al. (2011) and hints at a deviation from a flat spectrum (Figure 8). However, the points from Croll et al. (2011) and de Mooij et al. (2012) only differ from our derived radius ratio by  $1.5\sigma$  and  $1.1\sigma$ , suggesting that their data is in fact consistent with other published  $K$ -band observations. Differences between the transmission measurements could be a result of the use of different filters (i.e. our narrow-band  $H_2$  filter versus their broad-band  $K_s$  filter) and the correspondingly different wavelength coverage by the various groups. Our narrow-band filter probes a small wavelength range (FWHM =  $0.021 \mu\text{m}$ ) and is free of telluric features (Figure 2). The  $K_s$  transmission curve shown in Figure 2 is for the filter specifically used by Croll et al. (2011) and contains some telluric absorption features. While telluric effects should be largely removed by relative photometry, the choice of reference stars and their locations on the sky (relative to the target) can result in imperfect removal of telluric features. The  $K_s$ -band also contains some stellar lines, and we discuss this further in Section 5.3. Broad-band photometry therefore can be subject to additional systematics and yield less accurate measurements than narrow-band photometry. Ultimately, we find that  $K$ -band observations continue to support a high molecular weight atmosphere or a H-rich atmosphere with a cloud or haze layer over a cloud/haze-free H-rich atmosphere.

### 5.2. Constraints on a Cloudy/Hazy H-Rich Atmosphere

In the previous section, we concluded that  $K$ -band measurements are consistent with a flat transmission spectrum, which favors either a high molecular weight atmosphere or a H-rich atmosphere with a cloud or haze layer (Howe & Burrows 2012). However, the available  $K$ -band data does not have sufficiently high precision to discern between these two atmosphere models. Published  $B$ -band data (e.g., de Mooij et al. 2012, 2013; Narita et al. 2013; Teske et al. 2013) cannot definitively discriminate between these two scenarios either. In this section, we assume that the atmosphere is H-dominated [following the results from Valencia et al. (2013)], and we consider what constraints can be placed on a cloudy/hazy H-rich atmosphere.

For a H-rich atmosphere with relatively high number densities where collisions are frequent, collision-induced absorption (CIA) is a dominant source of opacity (Borysow 2002,

291 and references therein). Here, we consider a H-rich upper atmosphere that includes an  
 292 opaque cloud or haze layer at some low altitude/high pressure. We assume that any molec-  
 293 ular absorbers in the atmosphere are confined beneath a cloud/haze layer, and that the  
 294 atmosphere above the clouds/haze is metal-free as a result of some (photo)chemical or mix-  
 295 ing boundary (chemopause or homopause). If the H<sub>2</sub> envelope is sufficiently dense, it could  
 296 be detected by CIA in high-precision *K*-band spectrophotometry. This depends on tem-  
 297 perature, so the presence or absence of CIA features is also a constraint on temperature  
 298 (provided other conditions are met; see below). The equilibrium temperature of GJ 1214b  
 299 is  $\sim 500$  K (Charbonneau et al. 2009), but the upper atmosphere could be much hotter due  
 300 to XUV heating from the star (Lammer et al. 2013).

301 A condition for this model to hold is that the CIA opacity of H<sub>2</sub> dominates above the  
 302 pressure altitude of any cloud/haze layer present in the atmosphere (i.e.  $\tau_{H_2} \gtrsim 1$  above the  
 303 chemopause or homopause). Under this condition, we computed the minimum pressure ( $P_0$ )  
 304 at the top of a cloud/haze layer located in an isothermal atmosphere using the following  
 305 equation:

$$P_0 = k_B T \sqrt{\frac{1}{\sigma(T, \lambda) \sqrt{\pi R_0 H}}}. \quad (4)$$

306  $H$  is the scale height of the atmosphere, defined as

$$H = \frac{k_B T}{\mu g}, \quad (5)$$

307  $k_B$  is the Boltzmann constant,  $T$  is the atmospheric temperature,  $\mu$  is the mean molec-  
 308 ular weight of the atmosphere, and  $g$  is the planet’s surface gravity. We assumed  $T = 500$   
 309 K, and we set the reference planetary radius  $R_0 = 2.68 R_\oplus$ . We used H<sub>2</sub>-H<sub>2</sub> CIA opacities  
 310 ( $\sigma$ ) from Borysow (2002) and computed the scale height  $H$  using a mean molecular weight  
 311  $\mu = 2$  and a surface gravity  $g = 8.95 \text{ m s}^{-2}$ . From this, we computed the minimum pressure  
 312  $P_0$  at the top of the cloud or aerosol layer to be 60 mbar (at  $\lambda \sim 2.14 \mu\text{m}$ ). This minimum  
 313 pressure falls within the pressure range of 0.001–100 mbar considered by Howe & Burrows  
 314 (2012).

315 We then calculated the effective  $R_p/R_\star$  versus wavelength, following a similar procedure  
 316 as in Howe & Burrows (2012):

$$\frac{R_p}{R_\star} = \frac{R_0}{R_\star} + \frac{H}{2R_\star} \ln \left[ \frac{\sigma(T, \lambda)}{\sigma_0} \right]. \quad (6)$$

317 Here,  $R_0$  is the radius at the wavelength where  $\sigma = \sigma_0 = 2.78 \times 10^{-6} \text{ cm}^{-1} \text{ amagat}^{-2}$   
 318 at  $\lambda \sim 2.14 \text{ } \mu\text{m}$  [from the 500 K table from Borysow (2002)]. Because  $\text{H}_2$  absorption is  
 319 collisionally-induced, it depends on the square of the number density ( $n^2$ , where  $n$  = number  
 320 density of absorbers) and this leads to an additional factor of 1/2 in Eqn. 6 [compared to  
 321 the equation defined in Howe & Burrows (2012)].

322 Under the same conditions assumed above and using  $R_\star = 0.211 R_\odot$  (Charbonneau et al.  
 323 2009), we calculated the radius ratio for temperatures of 400, 500, 600, 700, 800, 900, and  
 324 1000 K. We compared the observed radius ratios to the predicted radius ratios by calculating  
 325  $\chi^2$  and identified the best-fit model (based on the minimum  $\chi^2$ ). Although the  $K_s$ -band data  
 326 from Croll et al. (2011) and de Mooij et al. (2012) are marginally consistent with other  $K$ -  
 327 band data within measurement uncertainties, we still considered them to be unexplained  
 328 outliers and excluded them from the analysis (Section 5.1).

329 We find the 400 K model had the smallest  $\chi^2$ , while the 1000 K model yielded the largest  
 330  $\chi^2$ . We show the 400 and 1000 K models in Figure 8. As the temperature increases, the  
 331 scale height increases, leading to additional absorption and a larger apparent planet radius;  
 332 however, the features also become washed out at higher temperatures. We computed  $\Delta\chi^2$   
 333 (relative to the minimum  $\chi^2$  at 400 K) and found that the deviation between the data and  
 334 models increases with increasing temperature. However,  $\Delta\chi^2$  between the 400 and 1000  
 335 K models is only  $\sim 0.72$ , since  $\chi^2$  is just 2–3 for all models. We conclude that from the  
 336 available data, we cannot exclude higher temperature atmospheres ( $T > 400 \text{ K}$ ) with any  
 337 confidence ( $p < 0.01$ ).

338 Considering the capabilities of future missions like the *James Webb Space Telescope*  
 339 (*JWST*) for high precision infrared spectroscopy, the atmosphere models were compared to  
 340 both the real data (using the actual measurement uncertainties) as well as an artificial data  
 341 set, consisting of the actual measurements with reduced errors. We defined artificial errors  
 342 so that the median error over the  $K$ -band data =  $1 \times 10^{-4}$  [based on the precision achieved  
 343 by Fraine et al. (2013) from *Spitzer* measurements of GJ 1214b at  $4.5 \text{ } \mu\text{m}$ ]. For comparison,  
 344 the median value of the actual errors is  $9.9 \times 10^{-4}$ . Based on the artificial high-precision  
 345 data, we again find that the 400 K model has the smallest  $\chi^2$ , and that  $\Delta\chi^2$  between the  
 346 400 and 1000 K models is 70.2, which would allow us to exclude atmospheres with  $T \geq 800$   
 347 K with  $> 99.7\%$  confidence ( $3\sigma$ ) assuming that we had such high precision data. We find  
 348 that a temperature of  $\leq 400 \text{ K}$  is preferred for a pure  $\text{H}_2$  upper atmosphere, but significantly  
 349 higher precision data (as well as more data in general) is needed to confidently exclude higher  
 350 temperature atmospheres.

351 Ultimately, while we find no evidence for deviation from a flat spectrum, a thin upper  
 352 atmosphere ( $\leq 60 \text{ mbar}$ ) dominated by  $\text{H}_2$  cannot be excluded. The possibility also remains

353 that there is simply no (or very little) H in the (upper) atmosphere.

354

### 5.3. Variability in the Stellar Spectrum

355

356

357

358

359

360

361

362

363

364

365

Fluorescent H<sub>2</sub> emission lines have been observed in the spectra of four planet-hosting M dwarf stars, but not in GJ 1214 (France et al. 2013). These lines are produced by photoexcitation by Ly $\alpha$  photons, and their detection indicates the presence of a 2000 – 4000 K molecular gas (France et al. 2013, and references therein). The H<sub>2</sub> filter is designed specifically to observe such lines, making it possible for us to also probe the stellar atmosphere with our observations. While France et al. (2013) do not detect Ly $\alpha$  emission in GJ 1214, they speculate that this is because the neutral H in GJ 1214’s atmosphere is instead contained in H<sub>2</sub> rather than H. Notably, GJ 1214 is the coolest star ( $T_{\text{eff}} \sim 3250$  K; Anglada-Escudé et al. 2013) in their sample, and H recombines at cool temperatures, so it is plausible that molecular H is present in GJ 1214’s atmosphere. This motivated us to look for H<sub>2</sub> emission in GJ 1214.

366

367

368

369

370

371

372

373

We examined a *K*-band spectrum of GJ 1214 from Rojas-Ayala et al. (2012), shown in Figure 9. We find no evidence of an H<sub>2</sub> emission feature around  $\sim 2.14$   $\mu\text{m}$  in GJ 1214’s spectrum. The H<sub>2</sub> line is close to the Brackett  $\gamma$  line (2.16  $\mu\text{m}$ ), which is produced in T Tauri stars by recombining magnetospheric gas (e.g., Hamann et al. 1988). However, we see no evidence of the Brackett  $\gamma$  line in the spectrum of GJ 1214. Indeed, the H<sub>2</sub> bandpass is free of any obvious stellar lines. The *K<sub>s</sub>* filter does include several stellar absorption lines, but assuming that these features are only present in the star (and are not telluric) and that they do not vary, these will not affect the photometry.

374

375

376

377

378

379

380

381

382

383

Due to the lower temperatures H<sub>2</sub> may predominate in star spots and may play an important role in the formation and evolution of spots (e.g., Jaeggli et al. 2012). Therefore, we also looked for evidence of H<sub>2</sub> variability, or patchiness in the stellar disk in the H<sub>2</sub> bandpass (either bright emission or dark absorption) which produces variability when transited by the planet (i.e. “H<sub>2</sub>-spots”).<sup>8</sup> We compared observations taken in-transit (when the time-varying part of the star is blocked by the planet’s disk) with those taken out-of-transit (when only the star light is visible). Specifically, we compared the rms scatter (of the light curve residuals, computed by subtracting the best-fit model from the data; Section 3.3) between the in-transit and out-of-transit windows for each of the seven individual transits. The resulting rms values are presented in Figure 10. We computed  $r^2 = 0.80$  between the in- and out-of-

---

<sup>8</sup>While we find no strong evidence of spot-crossing events in any of our light curves, we discuss a possible *bright* spot in Section 5.4.

384 transit rms, which indicates a strong linear correlation between the two parameters. That  
 385 a strong linear correlation exists suggests that the in- and out-of-transit measurements are  
 386 dominated by the same source of variation, i.e. photometric errors as opposed to a source of  
 387 variation associated with the transit alone. From this, we conclude that if H<sub>2</sub> is present and  
 388 absorbing or emitting in the stellar and/or planetary atmosphere, it is either not variable  
 389 or its variations are not detectable in our data. It is likely that the vibrational transitions  
 390 such as the 1-0 S(1) transition are too weak to be seen in a standard *K*-band spectrum (but  
 391 instead might be seen through a linearly polarized spectrum; White & Kuhn 2011).

392 The H<sub>2</sub> 1-0 S(1) line is also used to study molecular outflows from protostars (e.g.,  
 393 Garcia Lopez et al. 2013). We considered the possibility of detecting H<sub>2</sub> “outflows” from  
 394 the atmosphere of the planet (driven by UV heating), but we see no persistent deviations  
 395 from the standard transit light curve models that require explanation by a shock or wind  
 396 (i.e. from some massive atmospheric escape from the planet).

#### 397 5.4. Effects of Systematics

398 Systematics, whether astrophysical or instrumental in nature, can significantly affect  
 399 the derivation of light curve parameters. In this section, we describe potential sources of  
 400 systematics in our light curves and the effect they have on our measured radius ratios.

##### 401 5.4.1. Astrophysical Sources

402 Intrinsic variability of the host star can affect measurements of the radius ratio, and GJ  
 403 1214 has been shown to be variable at red ( $\sim 0.8 \mu\text{m}$ ) wavelengths at the 1-2% level over  $\sim$   
 404 1-2 year timescales (Carter et al. 2011). While we see no obvious visual evidence of stellar  
 405 flares or star spots<sup>9</sup> in our light curves (Figure 5), in principle it is possible to use the radius  
 406 ratios measured for the individual transits to estimate how much the spot coverage changed  
 407 with time. Theoretically, the shallowest observed transit should correspond to the stellar  
 408 surface being nearly free of spots, or at least having minimal spot coverage. As presented  
 409 in Table 3 and shown in Figure 7, the measured radius ratios do not vary significantly with  
 410 transit epoch. Between the photometric quality of the data and the magnitude of the errors

---

<sup>9</sup>When transited by the planet, the presence of a star spot would result in a brightening event in the light curve. When spots are present but are not transited by the planet, they reduce the overall brightness of the star and thus produce a deeper transit.

411 derived for the radius ratios, we cannot robustly identify a minimum epoch of stellar activity  
 412 based on the measured radius ratios. Based on the rms values presented in Figure 10, our  
 413 data suggest variability at a level of  $\sim 1.5 \times 10^{-3}$  (albeit only on hour-long timescales). We  
 414 also find that GJ 1214 is variable in the  $K$ -band at a level of  $\sim 0.5\%$  over longer timescales  
 415 (from August 2011 to July 2012 or  $\sim 1$  year), based on the target-to-reference flux ratio for  
 416 the most photometrically stable reference star in our sample. This is consistent with the  
 417 results from Carter et al. (2011), since stellar variability in our passband should be less than  
 418 the 1-2% measured by Carter et al. (2011) due to observing in a redder passband. Although  
 419 such variability does affect the measurement of radius ratios, since our radius ratios did not  
 420 vary significantly (within errors), we consider stellar variability to have a negligible effect on  
 421 our conclusions.

422 There is the possibility that spot-crossing events did occur in one or more of our observed  
 423 transits, but we simply cannot identify them by eye because they cause brightenings at or  
 424 below the level of our photometric precision. If we consider the red noise (Table 3) as a  
 425 measure of the effects of spot-crossing events, we find that the August 24, 2011 and June  
 426 16, 2012 transits have the highest levels of red noise. The June 16, 2012 transit had poorer  
 427 weather conditions, which is likely the cause of the higher red noise in that light curve,  
 428 as no evidence of a spot-crossing event is seen in that light curve. However, the August  
 429 24, 2011 transit, which had photometric conditions, does have an anomalous feature in its  
 430 light curve (Figure 11) where the transit depth appears to increase significantly immediately  
 431 before egress. The anomalous feature in the August 24, 2011 transit does not appear to be a  
 432 (dark) spot crossing event, since the transit depth before the feature occurred is consistent  
 433 (i.e. within  $1\sigma$ ) with the transit depth measured for the combined light curve (over all seven  
 434 transits). This suggests that the true transit depth should be based on the first part of the  
 435 transit, rather than the first part of the transit being a spot-crossing event.

436 To determine if this anomalous feature was produced by reference star variability, we  
 437 constructed alternative light curves using different reference stars. We found that the feature  
 438 was present in all cases. We also searched the literature to see if any other observations of  
 439 this specific transit had been published, but we only found an observation of the transit  
 440 following this one by Harpsøe et al. (2013). Their light curves do not appear to contain any  
 441 particularly anomalous features, which supports the idea of minimal (or at least un-transited)  
 442 spots at the time of the observations.

443 We also considered that the feature may instead be due to the planet passing over a  
 444 *bright* spot on the star, which would result in an increase in the transit depth, consistent  
 445 with our observations. However, the presence of a bright spot will also cause a *decrease* in  
 446 the unocculted transit depth. As illustrated in Figure 7, the transit depths measured for

447 all transits are consistent within  $1\sigma$ . This suggests that if the anomalous feature is a result  
 448 of a spot-crossing event, the spot is sufficiently compact/faint that it does not produce an  
 449 unocculted spot effect that we would detect. We do not find evidence of spot-crossing events  
 450 in our other transit observations, but we explore the bright spot hypothesis in more detail  
 451 here.

452 Assuming a circular spot with radius  $R_{\text{spot}}$ , we estimated the size of such a spot based  
 453 on the duration of the spot crossing,

$$\frac{R_{\text{spot}}}{R_{\star}} = \frac{t_{\text{spot}}}{\tau} \sqrt{1 - b^2}. \quad (7)$$

454 The transit duration ( $\tau$ ) is 52.73 min (Carter et al. 2011), and the spot-crossing time  
 455 ( $t_{\text{spot}}$ ) was estimated from the light curve to be 15 min (Figure 11). Using an impact  
 456 parameter ( $b$ ) of 0.28 (Bean et al. 2011), we computed a spot-star radius ratio of 0.27 (notably  
 457 over two times larger than  $R_p/R_{\star}$ ). We then computed how much the transit depth would  
 458 increase due to a bright spot (relative to the no spot case) from

$$\delta_f = B \left( \frac{R_{\text{spot}}}{R_{\star}} \right)^2. \quad (8)$$

459 This equation is applicable because our hypothetical spot is much larger than the planet.  
 460 The increase in the transit depth during the anomalous event relative to the depth prior to  
 461 the anomalous event is  $\Delta\delta = 0.0059$  (Figure 11). The transit depth ( $\delta_p$ ) is 0.0135.  $B$  is  
 462 the brightness enhancement of the spot relative to the rest of the stellar disk, which we  
 463 computed based on the relative depth of the anomalous feature, or  $B = \Delta\delta/\delta_p = 0.44$ .  
 464 From this, we calculate  $\delta_f = 0.033$ . This translates to a change in the transit depth due  
 465 to the unocculted bright spot of  $\delta_f \times \delta_p = 4.4 \times 10^{-4}$ , which is much smaller than our typical  
 466 photometric precision of  $1.7 \times 10^{-3}$  (for a single transit). It is also consistent with GJ 1214  
 467 being variable on the order of 1-2% (Carter et al. 2011). We conclude that a single transient  
 468 bright spot about twice the size of the planet’s disk could explain the transit of August 24,  
 469 2011. Regardless of the source of the feature, TAP recognized it as a systematic and derived  
 470 a radius ratio that is consistent with the radius ratios measured from the other transits  
 471 (Figure 7).



5.4.2. *Instrumental Sources*

Besides astrophysical systematics, we also considered the effect of instrumental systematics such as a nonlinear detector on our measured radius ratios. The WFCAM detector is linear to  $< 1\%$  up to about 40,000 counts per pixel.<sup>10</sup> To ensure that we avoided the defined non-linear regime, we measured the peak counts in the target and each reference star. We found that all stars remained below  $\sim 22,000$  counts (per pixel) in all observations. However, the possibility remains that lower non-linearity is present at lower counts (Section 2). To check this, we derived a “variance coefficient” ( $k$ ) for each reference star and for each night based on the following equation,

$$F_{\text{observed}} = F_{\text{actual}} - kF_{\text{observed}}^2. \quad (9)$$

Here,  $F_{\text{observed}}$  is the normalized flux ratio we measured for each reference star,  $F_{\text{actual}}$  is what the ideal flux ratio should be in the absence of systematics (i.e.  $F_{\text{actual}} \equiv 1$ ),  $k$  is defined as the variance coefficient, and  $F_{\text{observed}}^2$  is the variance of the observed flux ratio. After deriving  $k$  for each reference star and for each night, we found that on most nights,  $k \ll 1.1 \times 10^{-3}$ . Thus, we conclude that the effect of non-linearity is smaller than our photometric precision (typically  $1.7 \times 10^{-3}$  for a single transit). Only on two nights did the flux ratios have significant deviations: during the fifth transit (June 16, 2012) and sixth transit (June 27, 2012). That the fifth transit shows signs of non-linearity is consistent with the observations, since the stellar image was insufficiently defocused to avoid high counts. We have no explanation as to why the sixth transit is potentially affected by non-linearity. Given that the measured transit depth is consistent with those measured from the other individual transits, we conclude that any low-level non-linearity that might be present and a source of systematics has a minimal effect on our photometry.

5.5. **Treatment of Transit Model Parameters**

Finally, we considered how limitations in our knowledge of stellar properties affect the derived light curve parameters. In particular, there is a degeneracy between limb darkening and  $a/R_*$ , which in turn affects estimates of the stellar density, orbital eccentricity, and impact parameter. Furthermore, as Berta et al. (2012) point out, inaccurate treatment of limb darkening could introduce false absorption features into the transmission spectrum.

---

<sup>10</sup><http://apm49.ast.cam.ac.uk/surveys-projects/wfcam/technical/linearity>

500 Therefore, the accurate treatment of limb darkening is critical for precisely measuring light  
 501 curve parameters.

502 In the analyses described above, we held limb darkening coefficients and  $a/R_*$  fixed.  
 503 This decision was based on the fact that GJ 1214b’s transit duration is only 52 min and  
 504 the ingress/egress events last 6 min, compared to our cadence of  $\sim 1$  min. Having a rela-  
 505 tively small number of data points during ingress and egress makes it difficult to accurately  
 506 fit the limb darkening. However, Csizmadia et al. (2013) argue that stellar limb darken-  
 507 ing parameters should be fitted and not fixed in order to derive high-precision light curve  
 508 parameters. Thus, we used TAP to fit additional models to our data, with (1) limb dark-  
 509 ening as a free parameter and  $a/R_*$  held fixed, (2) limb darkening held fixed and  $a/R_*$  as  
 510 a free parameter, and (3) both limb darkening and  $a/R_*$  as free parameters. In all cases,  
 511 we fit a single radius ratio over all seven transits. For the models where limb darkening  
 512 was a free parameter (1 and 3), we derive linear and quadratic limb darkening coefficients  
 513 of  $(0.089\pm 0.018, -0.131\pm 0.018)$  and  $(0.090\pm 0.018, -0.130\pm 0.018)$ . Compared to the fixed  
 514 values that we used,  $(0.0475, 0.3502)$ , we find that the fitted linear coefficient is consistent  
 515 with the fixed coefficient within  $3\sigma$ , but the fitted quadratic coefficient differs from the fixed  
 516 coefficient by more than  $26\sigma$ . The derived value for  $a/R_*$  from model 2 ( $15.111^{+0.081}_{-0.080}$ ) is  
 517 consistent with the fixed value we used (14.975) within  $1.7\sigma$ . For model 3, we found  $a/R_* =$   
 518  $15.410 \pm 0.080$ , which differs from the fixed value by  $5.5\sigma$ . Despite differences between some  
 519 of the fixed and fitted parameters, we find that for all models, the derived radius ratios are  
 520 consistent within  $1\sigma$ . Specifically, the measured radius ratios for the three cases described  
 521 above are: (1)  $R_p/R_* = 0.1174\pm 0.0015$  when limb darkening is free and  $a/R_*$  is fixed, (2)  
 522  $R_p/R_* = 0.1157\pm 0.0013$  when limb darkening is fixed and  $a/R_*$  is free, and (3)  $R_p/R_* =$   
 523  $0.1175\pm 0.0013$  when both limb darkening and  $a/R_*$  are free. Recall that our base model  
 524 yielded  $R_p/R_* = 0.1158\pm 0.0013$  when keeping both limb darkening and  $a/R_*$  fixed. Since  
 525 all radius ratios are consistent within  $1\sigma$ , this indicates that fixing limb darkening as well as  
 526  $a/R_*$  did not significantly affect our results or conclusions.

527 **6. Conclusions**

528 In this paper, we presented results from seven transit observations of GJ 1214b acquired  
 529 in a narrow-band H<sub>2</sub> filter. Our analysis included a thorough technique for selecting reference  
 530 stars and incorporated light curve fits with red (correlated) noise. We measured a radius ratio  
 531 of  $0.1158\pm 0.0013$  when fitting the data from all seven transits together. This radius ratio is  
 532 consistent with previous *K*-band measurements, including those from Croll et al. (2011) and  
 533 de Mooij et al. (2012) which differ from ours by only  $1.5\sigma$  and  $1.1\sigma$ . We conclude that all

534 *K*-band data support a flat absorption spectrum for GJ 1214b, which suggests that either a  
535 high mean molecular weight atmosphere or a H-rich atmosphere with a cloud or haze layer  
536 is favored (Howe & Burrows 2012).

537 Since Valencia et al. (2013) find that the bulk amount of H/He in GJ 1214b’s volatile  
538 envelope is nonzero and could be as much as 7% by mass, we explored the scenario where GJ  
539 1214b has a H<sub>2</sub>-rich envelope and heavy elements are sequestered below a cloud or aerosol  
540 layer. After comparing models of a pure H<sub>2</sub> atmosphere with *K*-band observations, we find  
541 that we cannot exclude the possibility of a H<sub>2</sub>-rich upper atmosphere. It is difficult to disen-  
542 tangle different plausible atmosphere models in the *K*-band given the precision of available  
543 data and that the temperature of the upper atmosphere is otherwise unconstrained. We sug-  
544 gest that additional high-precision spectroscopic observations (from space) across the *K*-band  
545 would be most useful. High-precision measurements at short optical wavelengths ( $< 0.7 \mu\text{m}$ )  
546 would also be helpful in searching for evidence of Rayleigh scattering (e.g. de Mooij et al.  
547 2013; Narita et al. 2013), which would support a (cloudy/hazy) H-rich atmosphere for GJ  
548 1214b (Howe & Burrows 2012).

549 Finally, we explored variability due to H<sub>2</sub> in the stellar spectrum and investigated the  
550 effects of different systematics on our results, such as star spots, CCD non-linearity, and  
551 limitations in our knowledge of light curve parameters. Overall, we conclude that systematics  
552 did not significantly affect our photometry and that our results are robust to these effects.

553 While there is ample spectroscopic and photometric data available for this planet, much  
554 of the data comes from different instruments as well as analyses in addition to suffering from  
555 poor precision. This in itself introduces an additional systematic when comparing the data  
556 to atmosphere models. While beyond the scope of this paper, we conclude that a uniform  
557 analysis of all public data for GJ 1214b would be useful for establishing more robust limits  
558 on atmosphere models.

559 We are grateful to Mike Irwin and Mike Read for assisting us in accessing the WF-  
560 CAM data and illumination tables. We thank Norio Narita for helpful discussions on GJ  
561 1214b. We also thank Paul Wilson for providing data prior to publication. We acknowl-  
562 edge the anonymous referee for helping us improve this paper. This research was supported  
563 by NASA grants NNX10AI90G (Astrobiology: Exobiology & Evolutionary Biology) and  
564 NNX11AC33G (Origins of Solar Systems) to EG. The United Kingdom Infrared Telescope  
565 is operated by the Joint Astronomy Centre on behalf of the Science and Technology Facilities  
566 Council of the U.K. This research has made use of the VizieR catalogue access tool, CDS,  
567 Strasbourg, France.

## REFERENCES

568

569 Anglada-Escudé, G., Rojas-Ayala, B., Boss, A. P., Weinberger, A. J., & Lloyd, J. P. 2013,  
570 A&A, 551, A48

571 Bean, J. L., Miller-Ricci Kempton, E., & Homeier, D. 2010, Nature, 468, 669

572 Bean, J. L., Désert, J.-M., Kabath, P., et al. 2011, ApJ, 743, 92

573 Benneke, B., & Seager, S. 2012, ApJ, 753, 100

574 Berta, Z. K., Charbonneau, D., Bean, J., et al. 2011, ApJ, 736, 12

575 Berta, Z. K., Charbonneau, D., Désert, J.-M., et al. 2012, ApJ, 747, 35

576 Borysow, A. 2002, A&A, 390, 779

577 Carter, J. A., & Winn, J. N. 2009, ApJ, 704, 51

578 Carter, J. A., Winn, J. N., Holman, M. J., et al. 2011, ApJ, 730, 82

579 Casali, M., Lunney, D., Henry, D., et al. 2001, The New Era of Wide Field Astronomy, 232,  
580 357

581 Charbonneau, D., et al. 2009, Nature, 462, 891

582 Claret, A., & Bloemen, S. 2011, A&A, 529, A75

583 Croll, B., Albert, L., Jayawardhana, R., et al. 2011, ApJ, 736, 78

584 Crossfield, I. J. M., Barman, T., & Hansen, B. M. S. 2011, ApJ, 736, 132

585 Csizmadia, S., Pasternacki, T., Dreyer, C., et al. 2013, A&A, 549, A9

586 Cutri, R. M., Skrutskie, M. F., van Dyk, S., et al. 2003, "The IRSA 2MASS All-Sky Point  
587 Source Catalog, NASA/IPAC Infrared Science Archive.

588 de Mooij, E. J. W., Brogi, M., de Kok, R. J., et al. 2012, A&A, 538, A46

589 de Mooij, E. J. W., Brogi, M., de Kok, R. J., et al. 2013, arXiv:1305.5544

590 Désert, J.-M., Bean, J., Miller-Ricci Kempton, E., et al. 2011, ApJL, 731, L40

591 Eastman, J., Gaudi, B. S., & Agol, E. 2013, PASP, 125, 83

592 Fraine, J. D., Deming, D., Gillon, M., et al. 2013, ApJ, 765, 127

- 593 France, K., Froning, C. S., Linsky, J. L., et al. 2013, *ApJ*, 763, 149
- 594 Garcia Lopez, R., Caratti o Garatti, A., Weigelt, G., Nisini, B., & Antonucci, S. 2013, *A&A*,  
595 552, L2
- 596 Gazak, J. Z., Johnson, J. A., Tonry, J., et al. 2012, *Advances in Astronomy*, 2012, id. 697967
- 597 Hamann, F., Simon, M., & Ridgway, S. T. 1988, *ApJ*, 326, 859
- 598 Harpsøe, K. B. W., Hardis, S., Hinse, T. C., et al. 2013, *A&A*, 549, A10
- 599 Heng, K., & Kopparla, P. 2012, *ApJ*, 754, 60
- 600 Hodgkin, S. T., Irwin, M. J., Hewett, P. C., & Warren, S. J. 2009, *MNRAS*, 394, 675
- 601 Howe, A. R., & Burrows, A. S. 2012, *ApJ*, 756, 176
- 602 Jaeggli, S. A., Lin, H., & Uitenbroek, H. 2012, *ApJ*, 745, 133
- 603 Lammer, H., Erkaev, N. V., Odert, P., et al. 2013, *MNRAS*, 430, 1247
- 604 Lépine, S., & Gaidos, E. 2011, *AJ*, 142, 138
- 605 Kundurthy, P., Agol, E., Becker, A. C., et al. 2011, *ApJ*, 731, 123
- 606 Mandel, K., & Agol, E. 2002, *ApJ*, 580, L171
- 607 Menou, K. 2012, *ApJ*, 744, L16
- 608 Miller-Ricci, E., & Fortney, J. J. 2010, *ApJL*, 716, L74
- 609 Miller-Ricci Kempton, E., Zahnle, K., & Fortney, J. J. 2012, *ApJ*, 745, 3
- 610 Morley, C. V., Fortney, J. J., Kempton, E. M.-R., et al. 2013, *arXiv:1305.4124*
- 611 Murgas, F., Pallé, E., Cabrera-Lavers, A., et al. 2012, *A&A*, 544, A41
- 612 Narita, N., Nagayama, T., Suenaga, T., et al. 2012, *arXiv:1210.3169*
- 613 Narita, N., Fukui, A., Ikoma, M., et al. 2013, *arXiv:1305.6985*
- 614 Pierrehumbert, R. T. 2010, *Principles of Planetary Climate*, by R. T. Pierrehumbert. Cam-  
615 bridge, UK: Cambridge University Press. ISBN: 9780521865562, 2010
- 616 Roeser, S., Demleitner, M., & Schilbach, E. 2010, *AJ*, 139, 2440
- 617 Rojas-Ayala, B., Covey, K. R., Muirhead, P. S., & Lloyd, J. P. 2012, *ApJ*, 748, 93

- 618 Rogers, L. A., & Seager, S. 2010, *ApJ*, 716, 1208
- 619 Schneider, J., Dedieu, C., Le Sidaner, P., Savalle, R., & Zolotukhin, I. 2011, *A&A*, 532, A79
- 620 Skrutskie, M. F., Cutri, R. M., Stiening, R., et al. 2006, *AJ*, 131, 1163
- 621 Stead, J. J., & Hoare, M. G. 2011, *MNRAS*, 418, 2219
- 622 Teske, J. K., Turner, J. D., Mueller, M., & Griffith, C. A. 2013, *MNRAS*, 431, 1669
- 623 Valencia, D., Guillot, T., Parmentier, V., & Freedman, R. S. 2013, arXiv:1305.2629
- 624 White, A., & Kuhn, J. R. 2011, *Bulletin of the American Astronomical Society*, 43, #436.02
- 625 Zacharias, N., Finch, C. T., Girard, T. M., et al. 2013, *AJ*, 145, 44

Table 1. Transit Observations

Date (UT)	Start Time (UT)	End Time (UT)	Airmass Start	Airmass End	Notes
2011-08-05	07:03:04.3	10:03:04.3	1.04	1.58	(a)
2011-08-24	05:50:47.0	08:51:30.2	1.04	1.61	
2012-04-28	09:18:43.2	13:01:55.2	1.89	1.03	
2012-05-17	07:57:13.0	11:30:02.9	1.98	1.04	
2012-06-16	08:21:33.1	11:50:12.5	1.13	1.17	(b)
2012-06-27	09:51:50.4	13:13:09.1	1.05	2.01	
2012-07-05	07:43:14.9	11:11:19.7	1.07	1.29	(c)

<sup>(a)</sup>Conditions were windy throughout the observations.

<sup>(b)</sup>Conditions were mixed (thin/thick clouds), and an incorrect focus setting was used in the beginning of the observations (resulting in saturation), so the first part of the observations was discarded. See Section 3 for further details.

<sup>(c)</sup>Conditions were windy through the first half of the observations.

Table 2. Fixed Transit Model Parameters<sup>a</sup>

Parameter	Value	Reference
$P$ (days)	1.58040481	Bean et al. (2011)
$i$ (deg)	88.94	Bean et al. (2011)
$a/R_*$	14.9749	Bean et al. (2011)
$\mu_1^b$	0.0475	Claret & Bloemen (2011)
$\mu_2^b$	0.3502	Claret & Bloemen (2011)

<sup>(a)</sup>A circular orbit is assumed.

<sup>(b)</sup>The linear and quadratic limb darkening coefficients are for the  $K$ -band.



Table 3. Best-Fit Model Parameters

Date (UT)	$T_{\text{mid}}$ (JD-2450000)	White Noise	Red Noise	$R_p/R_*$ <sup>a</sup>
2011-08-05	5778.84962 +0.00025 -0.00026	0.00122 +0.00015 -0.00017	0.0093 +0.0026 -0.0023	0.1161 +0.0047 -0.0048
2011-08-24	5797.81581 +0.00024 -0.00024	0.00048 +0.00017 -0.00026	0.0109 +0.0015 -0.0015	0.1162 +0.0040 -0.0041
2012-04-28	6045.93714 +0.00024 -0.00024	0.00106 +0.00012 -0.00013	0.0084 +0.0020 -0.0017	0.1152 +0.0034 -0.0036
2012-05-17	6064.90099 +0.00018 -0.00018	0.00104 +0.00010 -0.00011	0.0050 +0.0020 -0.0019	0.1133 +0.0026 -0.0028
2012-06-16	6094.92825 +0.00046 -0.00044	0.00169 +0.00038 -0.00046	0.0174 +0.0053 -0.0057	0.1224 +0.0073 -0.0078
2012-06-27	6105.99128 +0.00022 -0.00021	0.00090 +0.00013 -0.00015	0.0076 +0.0021 -0.0020	0.1153 +0.0031 -0.0032
2012-07-05	6113.89391 +0.00019 -0.00019	0.00109 +0.00010 -0.00010	0.0059 +0.0019 -0.0016	0.1176 +0.0028 -0.0028

<sup>(a)</sup>The best-fit radius ratio from fitting all seven transits together is  $0.1158 \pm 0.0013$ . The best-fit radius ratios from fitting the seven transits separately are shown in the fifth column and are also shown in Figure 7. See text for further details.

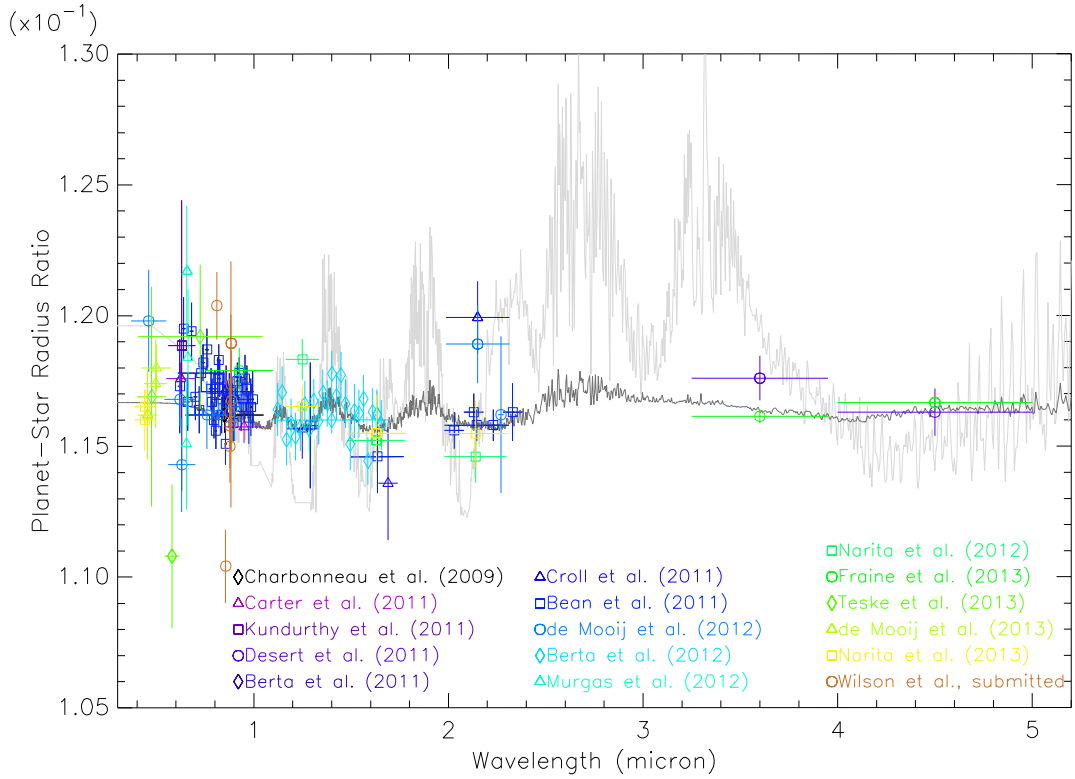


Fig. 1.—  $R_p/R_\star$  from published observations of GJ 1214b. The horizontal error bars on each point indicate the approximate bandpass for each observation. The data points are color-coded according to the source they were retrieved from and are shown in order of publication date. Also shown are two atmosphere models from Howe & Burrows (2012) that best fit a majority of the data published by 2012. The light gray line is a model for a solar composition atmosphere with a tholin haze at 10-0.1 mbar composed of  $0.1 \mu\text{m}$  particles with a particle density of  $100 \text{ cm}^{-3}$ . The dark gray line is a model for an atmosphere with a composition of 1%  $\text{H}_2\text{O}$  and 99%  $\text{N}_2$  and with a tholin haze at 0.1-0.001 mbar composed of  $0.01 \mu\text{m}$  particles with a density of  $10^6 \text{ cm}^{-3}$ .

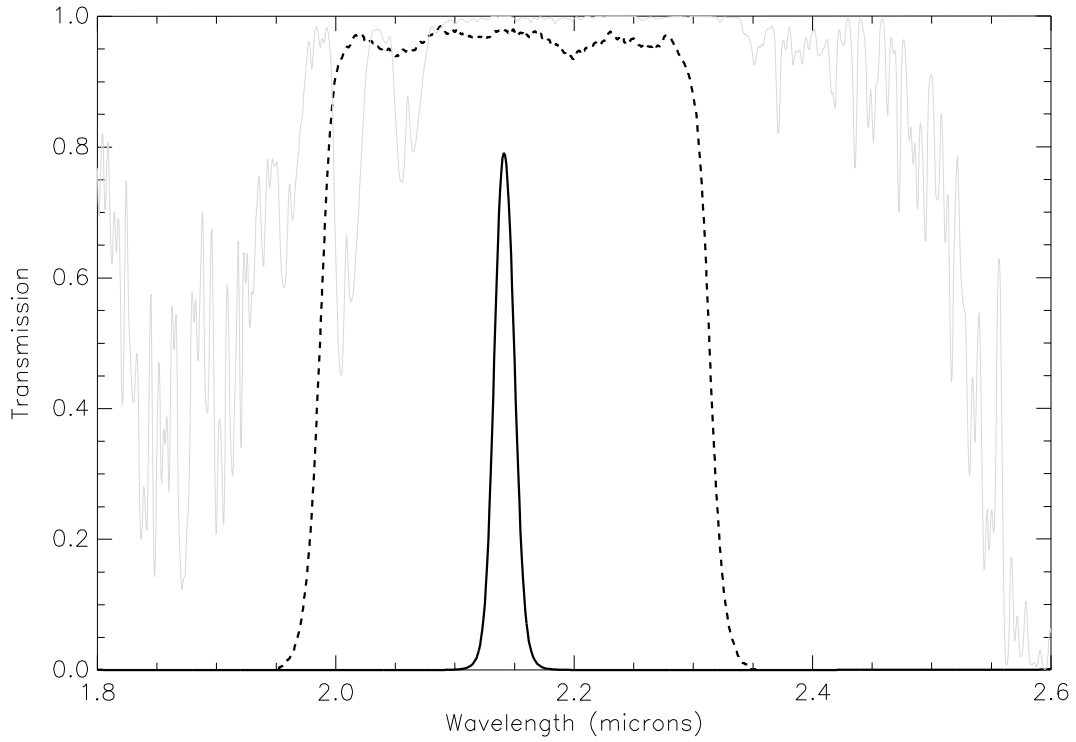


Fig. 2.— Transmission profiles of the narrow-band H<sub>2</sub> filter (solid line), broad-band  $K_s$  filter (dashed line), and atmosphere above Mauna Kea Observatory at an airmass of 1 and with a water vapor column of 1.2 mm (solid gray line).

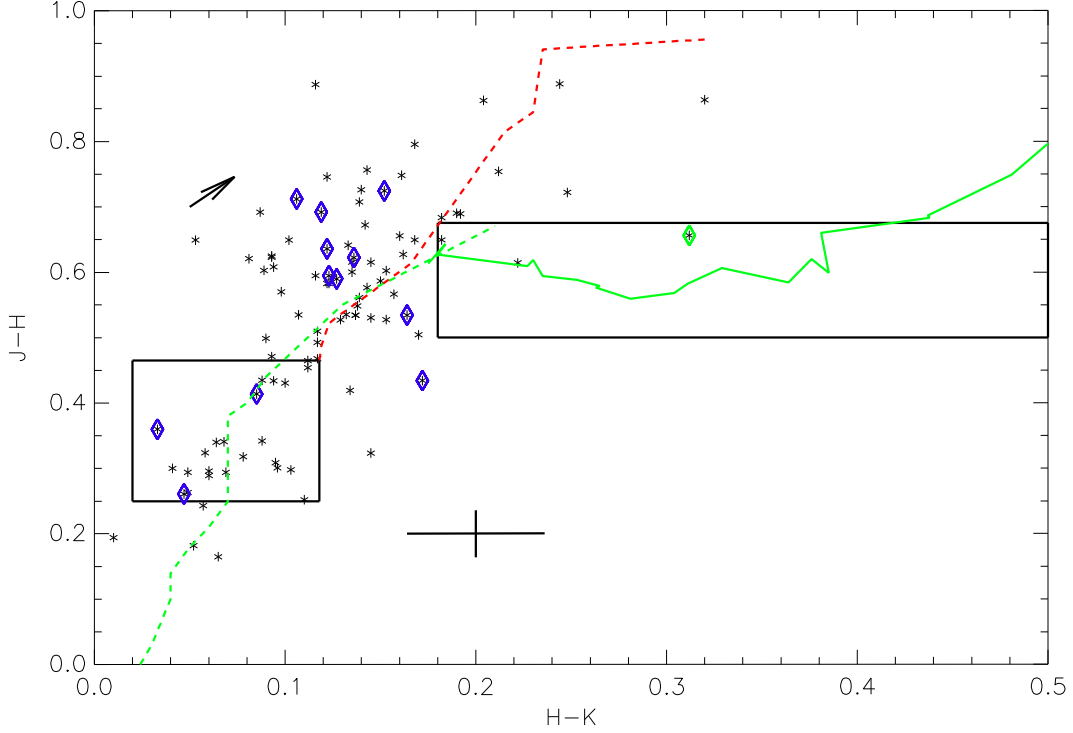


Fig. 3.— Infrared color-color diagram of stars in the vicinity of GJ 1214 (on the plane of the sky) and with  $K$ -band magnitudes between 8.282 and 10.782 ( $K = 8.782$  for GJ 1214). The horizontal and vertical black lines indicate the typical error in the colors, and the black arrow indicates the interstellar reddening vector. The dashed green curve is the 2MASS main-sequence locus from Stead & Hoare (2011), the solid green curve is a main-sequence locus for later type stars, and the dashed red curve is the 2MASS giant locus. GJ 1214 is marked with a small green diamond. The two regions marked by black rectangles are where some reference stars were selected based on the location of the main-sequence locus. The locations of the boxes were chosen to avoid the giant locus. The upper right corner of the selection box on the left side of the figure is located at the colors of a G5 III star, the bluest common giant. The twelve comparison stars that were used for relative photometry based on color and reduced proper motion criteria from Lépine & Gaidos (2011), their proximity to the main-sequence locus, and their location in the sky (i.e. in the WFCAM FOV) are marked with small blue diamonds. See text for further details.

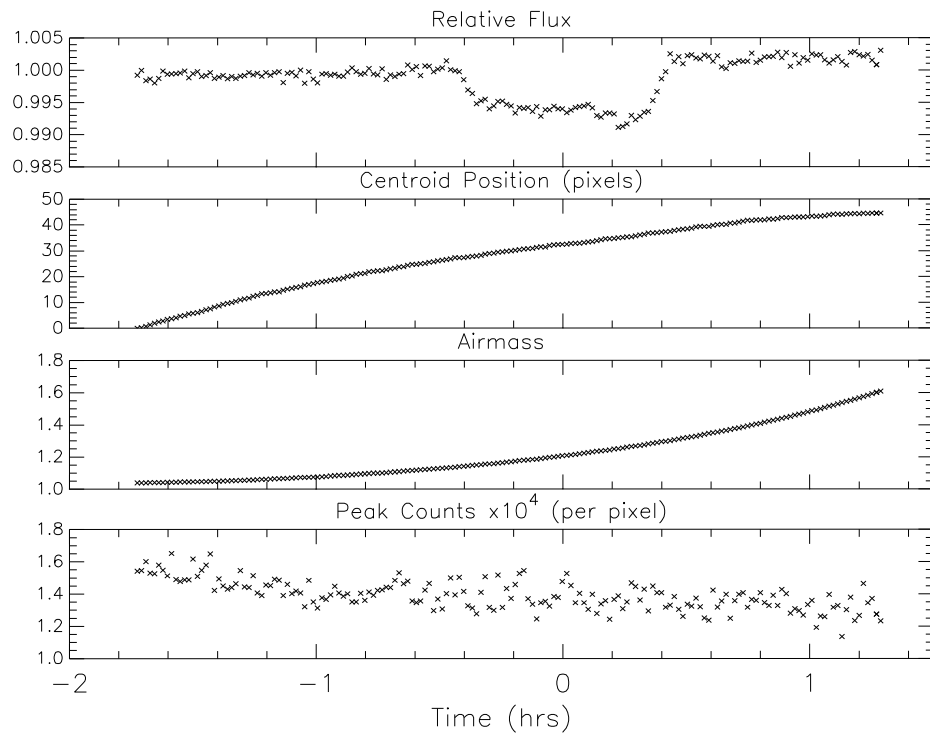


Fig. 4.— Plots of the raw light curve (relative flux versus time) for the August 24, 2011 transit of GJ 1214b (top panel), along with parameters used for detrending the light curve (bottom panels). The centroid position and peak counts shown are for the target. The detrended light curve is plotted in Figure 5.

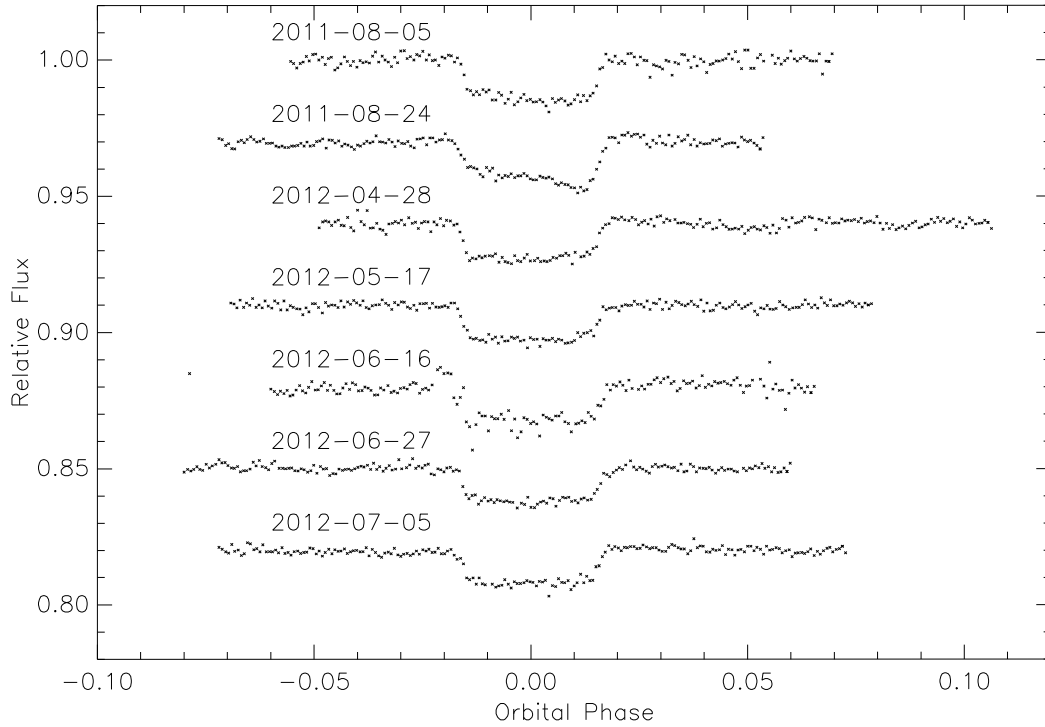


Fig. 5.— Detrended light curves for each of the seven observed transits of GJ 1214b. The light curves have been offset for clarity. Each light curve has been corrected against linear trends in the target centroid position, airmass, and the peak counts in the target (per pixel). See Figure 4 for an example of the parameters used to detrend the light curves.

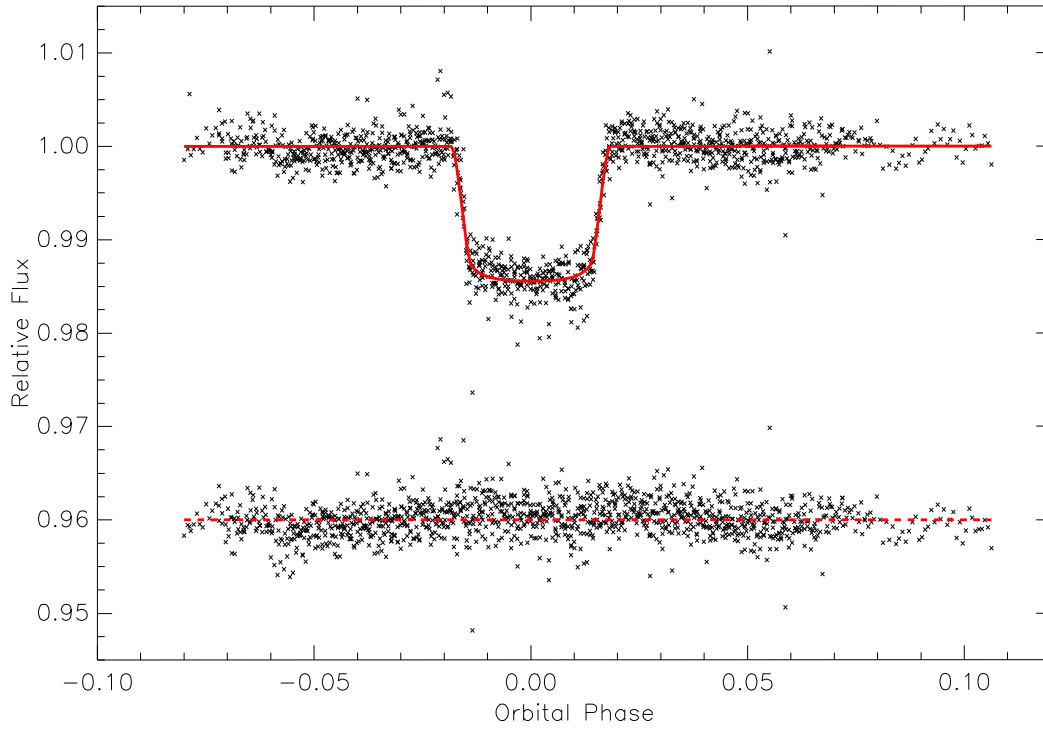


Fig. 6.— Combined light curve (black points), best-fit model (solid red curve), and light curve residuals (offset black points) of transits of GJ 1214b. The light curve shown is a combination of the data from all seven transits shown in Figure 5. The solid red curve is a best-fit model based on fitting a single radius ratio over all transits. The light curve residuals after removing the model from the data are offset for clarity and have an rms of  $2.0 \times 10^{-3}$ . See text for further details.

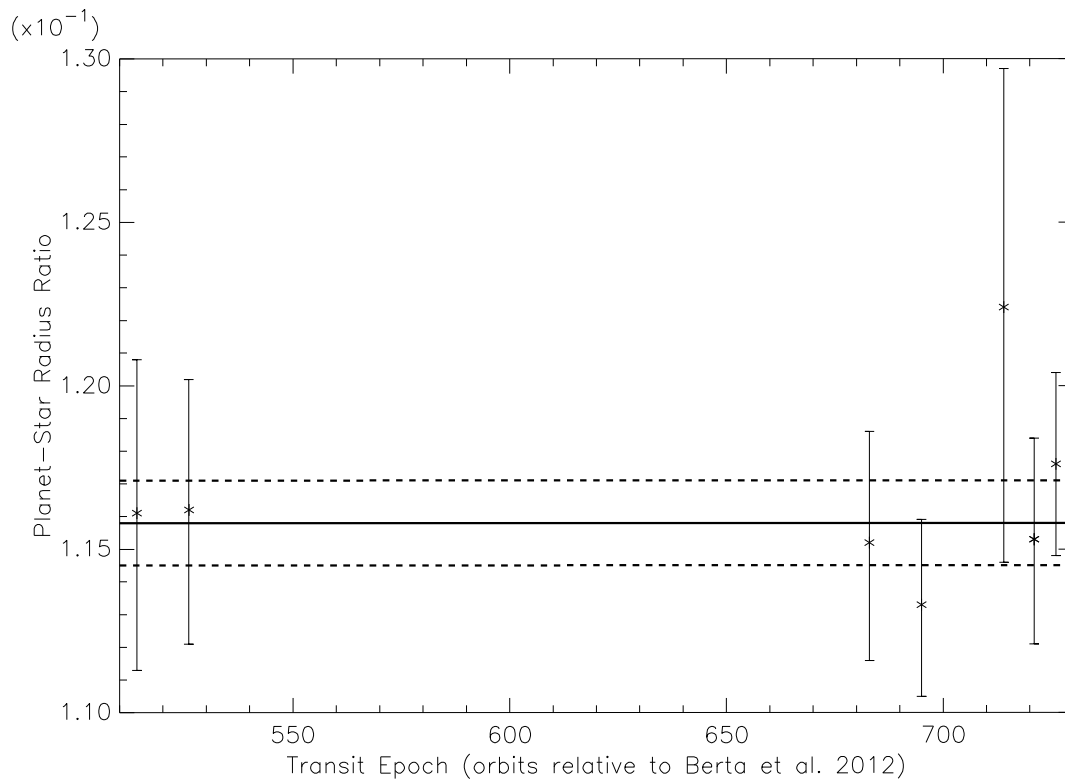


Fig. 7.— Best-fit radius ratios derived from TAP models fit to the data. We show the best-fit radius ratios and their corresponding  $1\sigma$  uncertainties from fitting the seven transits separately versus transit epoch based on the ephemeris from Berta et al. (2012). The solid line is the best-fit radius ratio from fitting all seven transits together (with the  $\pm 1\sigma$  uncertainties shown as dashed lines).



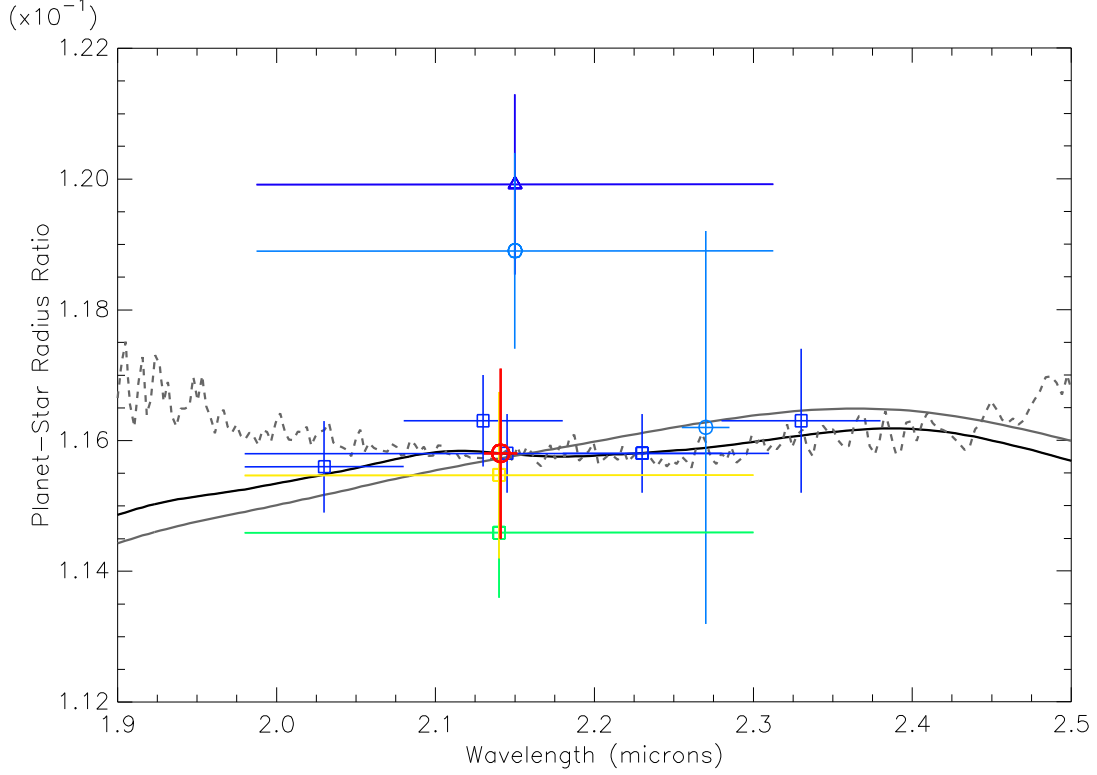


Fig. 8.—  $R_p/R_*$  from our analysis (red circle) compared to others published in the literature. The symbols are the same as in Figure 1: the blue triangle is from Croll et al. (2011), blue squares are from Bean et al. (2011), blue circles are from de Mooij et al. (2012), the green square is from Narita et al. (2012), and the yellow square is from Narita et al. (2013). Vertical error bars are one standard deviation. The horizontal error bars on each point indicate the approximate bandpass of the filter used for each observation. The solid black and gray curves are 400 and 1000 K pure  $H_2$  atmosphere models. The models have been offset by a reference radius ratio,  $R_0/R_*$ , derived from fitting the models to the data. The 400 and 1000 K models were found to have the lowest and highest  $\chi^2$  values [after comparing atmosphere models with different temperatures with the  $K$ -band data, excluding the outlying Croll et al. (2011) and de Mooij et al. (2012)  $K_s$ -band data]. The 470 K 1%  $H_2O$  and 99%  $N_2$  plus haze atmosphere model from Howe & Burrows (2012) shown in Figure 1 as the dark gray curve is also shown here as a dashed gray curve.

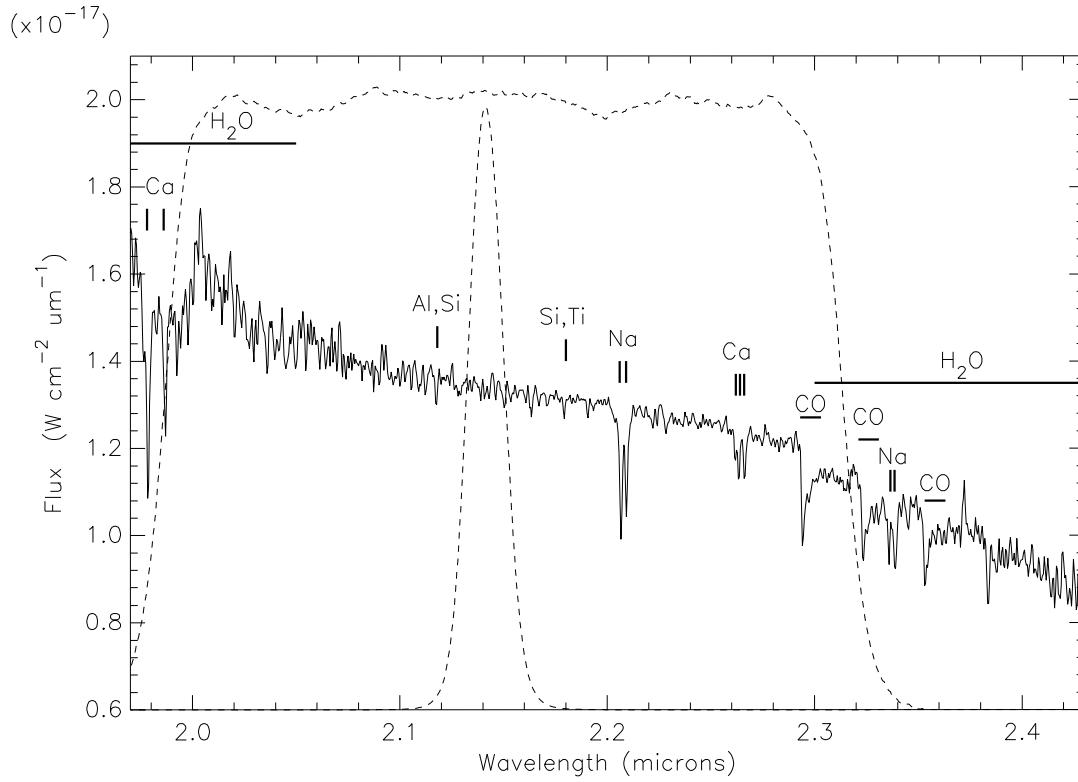


Fig. 9.—  $K$ -band spectrum of GJ 1214 from Rojas-Ayala et al. (2012). Pronounced stellar absorption lines are labeled. The profiles of the narrow-band  $\text{H}_2$  filter and the  $K_s$  filter are illustrated by the dashed curves.

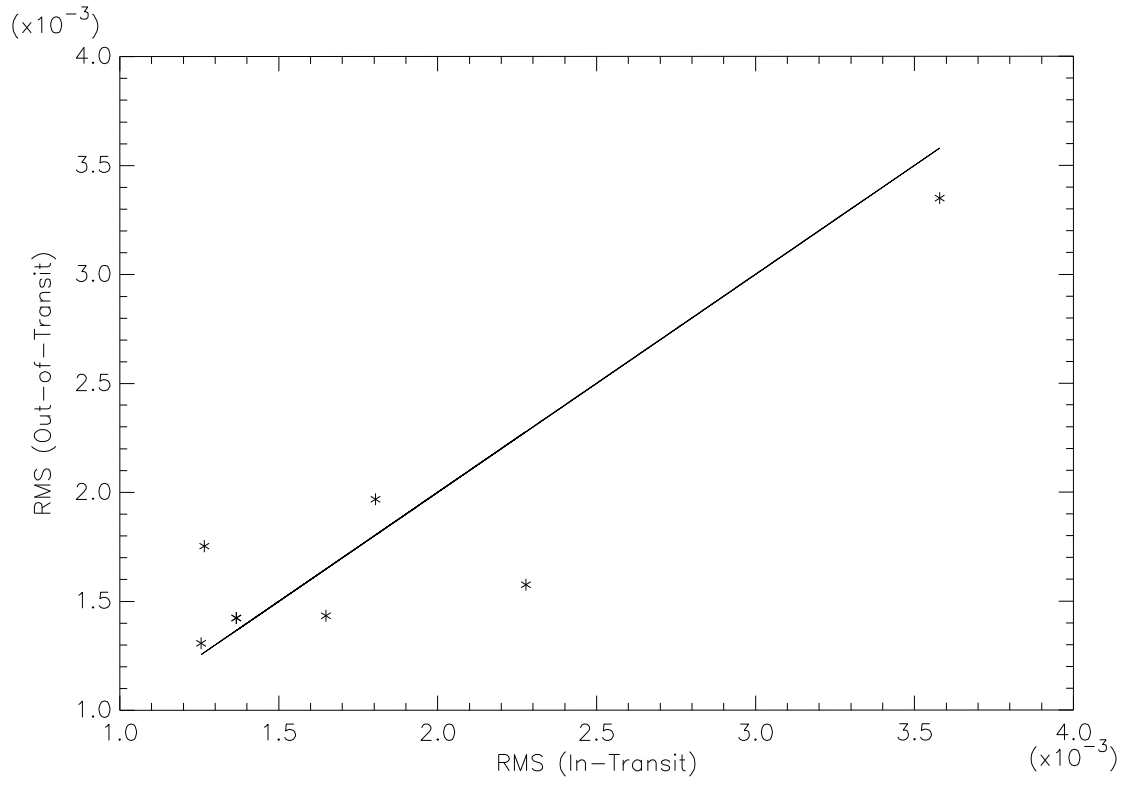


Fig. 10.— The in-transit rms versus out-of-transit rms for each observed transit. The solid line illustrated equality between the in- and out-of-transit rms values.

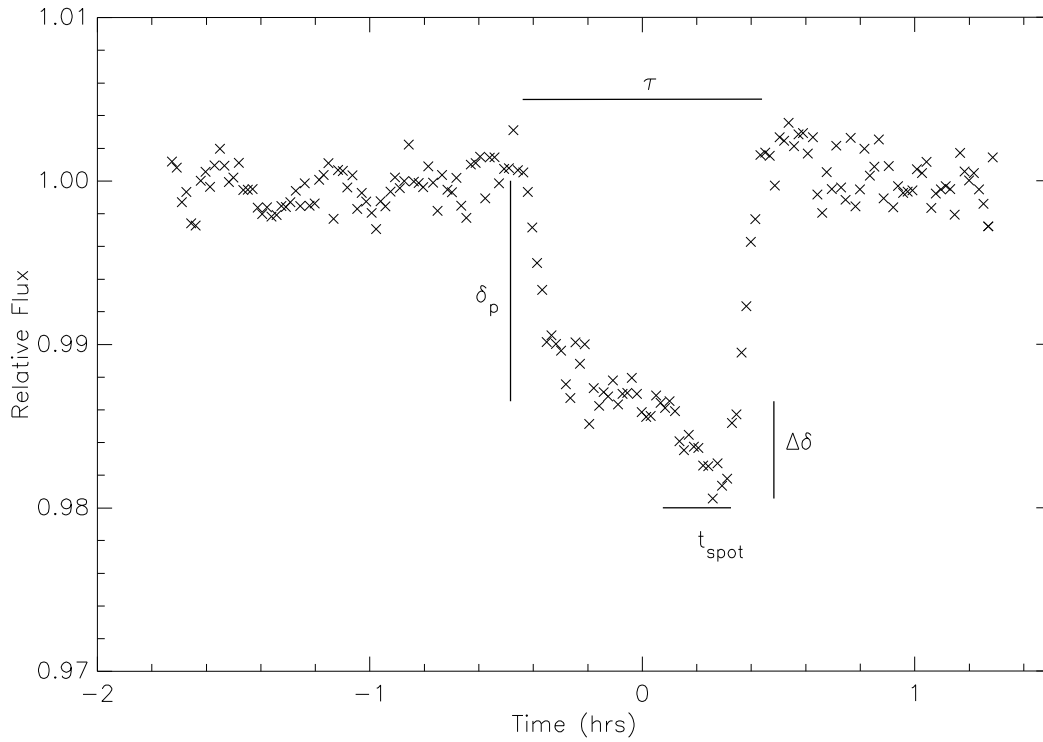


Fig. 11.— Light curve for the August 24, 2011 transit of GJ 1214b. The intervals for the transit duration  $\tau$  and the crossing time of a hypothetical bright spot  $t_{spot}$  are marked with horizontal black lines. The vertical black lines indicate the depth of the planetary transit ( $\delta_p$ ) and the change in the transit depth due to the anomalous feature ( $\Delta\delta$ ).